

<https://doi.org/10.1038/s41536-025-00434-x>

Optical mapping of the interface between iPSC-derived grafts and swine myocardium suggests potential arrhythmia mechanisms

Check for updates

Bijay Guragain^{1,3}, Hanyu Zhang^{1,3}, Yuhua Wei¹, Lei Ye¹, Gregory P. Walcott^{1,2}, Jack M. Rogers¹✉ & Jianyi Zhang^{1,2}✉

We used high-resolution optical mapping (~50 μm) to investigate potential arrhythmia mechanisms following transplantation of engineered cardiac tissue. We induced myocardial infarction in 6 immunosuppressed pigs and implanted cardiac spheroids into the border zone. One week later, 600-μm-thick cardiac slices containing implanted spheroids were harvested and electrical propagation was imaged. Histology showed low connexin-43 expression, scar, and misaligned muscle fibers at the graft-host interface. We observed propagation from host-to-graft in 10 slices from 3 pigs. Host-graft electrical bridges were spaced by millimeters. Propagation was ~4-fold slower in the graft than host. One graft beat spontaneously, but activation did not propagate from graft-to-host in this, or any other slice. We did not observe reentry, but slow in-graft conduction and sparse electrical bridges provided opportunity for reentry induction. These data reveal potential for reentrant or focal arrhythmias 1 week post-implant, which may resolve with maturation of the graft and the graft-host interface.

Despite ongoing improvements in the management of cardiac disease, patients with severe acute myocardial infarction (MI) often progress to end-stage congestive heart failure, which remains one of the most significant problems in public health. From the molecular and cellular perspective, heart failure is caused by the loss of cardiomyocytes (CMs), the fundamental contractile units of the heart¹, and because mammalian cardiomyocytes exit the cell cycle shortly after birth, cardiomyocytes in the hearts of adult mammals cannot proliferate in response to injury^{1,2}. One strategy to replenish lost CMs, remuscularization of damaged myocardium using grafts of CMs differentiated from human induced pluripotent stem cells (hiPSC-CM), has shown promising results, including improved cardiac function and reduced scar size^{3–7}. However, whether, and to what extent, the engrafted CMs electrically couple with endogenous cardiomyocytes remains poorly understood. Poor coupling can both impair contractile function and increase the risk of graft-associated lethal arrhythmias.

We recently published a brief report demonstrating that one week after hiPSC-CM spheroids were injected into the infarcted hearts of immunosuppressed pigs, in slices of myocardium harvested from the hearts, a

substantial number of the transplanted cells were engrafted, electrically active, and coupled with the native myocardium⁸. Electrical activation of host and graft tissue could remain synchronized at rates of up to 4 Hz⁸. Notably, in that study, we did not investigate whether electrical activity in the engrafted spheroids could be conducted back to the host cells, the propensity of the spheroids to generate arrhythmias, nor the spatial density of electrical bridges between host and graft. Post-transplant graft-associated arrhythmias, known as engraftment arrhythmias (EAs)⁹, have been frequently observed in clinically-relevant large animal models¹⁰, posing a serious safety concern for clinical translation. Several EA mechanisms have been speculated, including reentry circuits, graft automaticity, and triggered activity. However, the operative mechanisms remain unclear, partly due to the lack of a technical platform to examine intramural graft-host electrical interaction with sufficient spatiotemporal resolution¹¹.

In our previous study⁸, we developed a method for obtaining organotypic slices of host swine myocardium containing engrafted spheroids one week after implant. The spheroids were labeled with a genetically encoded calcium indicator (GECI) and the entire slice was stained with an

¹Department of Biomedical Engineering, School of Medicine and School of Engineering, University of Alabama at Birmingham, Birmingham, AL, USA. ²Department of Medicine/Cardiovascular Diseases, University of Alabama at Birmingham, Birmingham, AL, USA. ³These authors contributed equally: Bijay Guragain, Hanyu Zhang. ✉e-mail: jrogers@uab.edu; jayzhang@uab.edu

organic voltage-sensitive fluorescent dye (VSD). This enabled us to image electrical propagation in the host-spheroid system with high spatiotemporal resolution and to unambiguously distinguish electrical activation of the grafts from that of the host. In the present study, to shed light on the mechanisms of EAs, we sought to document electrical activation propagating from the engrafted tissue into the host and to examine the potential for spheroid involvement in arrhythmogenesis.

Results

We obtained a total of 57 tissue slices from the 6 pigs 1 week post-implantation. Twenty two of them contained electrically active grafts as identified by CaT imaging. Six of the slices with grafts were obtained from pigs 1 and 2. They were not analyzed for electrical coupling with dual Vm-CaT mapping because they were obtained during the initial study phase when only single-channel CaT mapping instrumentation was available. Electrically active spheroids were not found in any slices from the third pig. The remaining 16 slices that contained electrically active spheroids were obtained from the remaining 3 pigs. These slices were all imaged with dual Vm-CaT mapping.

Among the 16 dual-mapped slices, electrical coupling between the host myocardium and engrafted spheroids was found in a total of 10 slices obtained from all 3 pigs. This coupling was detailed in our previous brief report⁸. In one of these pigs, the spheroids were implanted with parallel injection, which resulted in a slice with a large elongated graft nearly 1 cm in length (Fig. 1A). In the remaining two pigs, implantation was by perpendicular injection, and slices contained roughly circular grafts of sub-millimeter to millimeter scale.

Potential Reentry in Large Grafts

Figure 1A is a fluorescence image of the myocardial slice with the hiPSC-CM graft region indicated with blue shading. The slice was stimulated using remote bipolar pacing at site P. At a pacing rate of 0.5 Hz, the electrical wave entered the graft from the surrounding host at a single site (site 2 in Fig. 1A). The wave then propagated through the graft towards both of its ends (sites 1 and 3; Fig. 1B, C; Supplementary Movie 1). With 1.5 Hz pacing, propagation entered the graft at the same site, but the wave propagated in only one direction, toward site 1. On every other stimulus, the wave failed part way to site 1. (Fig. 1D–F; Supplementary Movie 2). With pacing 3 Hz and above, electrical propagation could no longer be sustained through the host-graft connection and no electrical activation of the graft was observed. The responses of the graft to the other pacing rates (1 Hz and 2 Hz) were intermediate and are shown in Supplementary Fig. S1 and Supplementary Movies 3 and 4.

Table 1 shows electrical parameters measured in this slice at the different pacing rates. Included are propagation velocity in the host and graft, their ratio (α), APD, and wavelength (λ). It is worth noting that BDM is known to shorten APD¹², so this parameter is likely underestimated in our preparation. Wavelength is defined as the product of conduction velocity and refractory period and characterizes the spatial distance between the wavefront and the repolarizing wave-back. We estimated this parameter in the host myocardium using APD as a surrogate for the refractory period. APD is commonly used to approximate the refractory period, especially in well-perfused tissue. Although refractoriness can extend beyond repolarization, this generally occurs as a result of ischemia or drugs¹³.

Importantly, we never observed propagation leaving the graft and entering the host myocardium. The electrical wave entered the graft from only one site and propagated to one or two dead ends. Propagation from site 2 to site 1 was in the opposite direction as propagation in the host myocardium. Because of the slow conduction speed in the graft, at slower pacing rates, when the wave reached the dead end in the graft, the surrounding host myocardium had repolarized (Supplementary Movies 1 and 3). Had the wave left the graft and propagated back into the host tissue, graft-associated arrhythmia could have been established: specifically, a reentrant circuit with propagation repeatedly cycling from host-to-graft and graft-to-host¹⁴.

Figure 2 shows immunofluorescence images of serial 10 μ m-thick sections taken from the slice. The section shown in panels A and B was

stained for human-specific KU80 (red), DAPI, and α -SA and indicates the position of the graft, which was nearly 1 cm in length. In the adjacent section, shown in panels C–F, CX43 (red) staining replaced KU80. This section is also shown in Supplementary Fig. S2, with different regions magnified. Supplementary Fig. S3 shows H&E staining of the next section. In the host myocardium, the muscle fiber orientation (indicated by α -SA) was highly organized; in the graft tissue, the muscle fiber orientation was less organized and roughly aligned with the needle track, which is transverse to surrounding host myocardial fibers (Fig. 2B; Supplementary Figs. S2 and S3). Scar tissue (containing non-myocytes that stained positive for DAPI but negative for α -SA) was abundant along the host-graft interface (Fig. 2B, D, F). In Supplementary Fig. S3B, D, there are buffer regions hundreds of microns long that lack contact between cardiac myocytes in the graft and host. Gap junction protein CX43 expression was more prevalent and more organized in the host myocardium than in the graft (Fig. 2C–F; Supplementary Fig. S2). CX43 expression appearing to connect graft and host was rare and only clearly observed at the site indicated by the arrow in Fig. 2D–F. This site may be the entry site of the propagating wave from the host into the graft (site 2) in Fig. 1.

Figure 3 shows another slice with a relatively large graft approximately 2 mm in diameter (panel A, blue-shaded region). This graft resulted from perpendicular spheroid injection. The progression of activation in the host myocardium (Vm) and graft (CaT) in response to 1 Hz remote bipolar pacing are illustrated in panels B, C and Supplementary Movie 5. Activation entered the graft at the top-left corner and the bottom-right edge and spread to the left and right. Like the slice in Fig. 1, we did not observe activation leaving the graft and re-entering the host.

Figure 3D shows immunohistology imaging similar to that shown in Fig. 2 of a cryosection taken from the slice from Fig. 3A–C. At most points along the graft-host interface, the tissue was separated by non-myocyte tissue. In this slice, we identified just two potential coupling sites where CX43 appeared to bridge host and graft myocytes. One such site is shown in panel D (V, VI). It is likely site 1 in Panel A at which electrical activation entered the graft. The other site is shown in Supplementary Fig. S4. It is about 2 mm away and may be site 2 in Panel A.

Graft automaticity

All myocardial slices with detected grafts from the 3 dual-mapped pigs were optically mapped without pacing to identify spontaneous graft activation. We found automaticity in only one slice. In the heart the slice was taken from, the spheroids were implanted with perpendicular injection. Figure 4 shows an example of automaticity. The graft is indicated by a blue circle in panel A. The spontaneous rate was \sim 0.75 Hz (panel B, CaT signal). We did not observe functional coupling between the graft and the host myocardium: Spontaneous beats never propagated from the graft to the host myocardium (panel B, Vm signal). Conversely, during remote bipolar pacing, the host tissue activated (panel C, Vm signal), but the graft did not (panel C, CaT signal).

Similarly to the slice in Figs. 2 and 3, we imaged a cryosection from this slice with immunohistology for DAPI, KU80, and α -SA (Fig. 4D[I, II]). It was then de-stained and re-stained for DAPI, CX43, and α -SA (Fig. 4D[III, IV]). A graft about 200 μ m in diameter was observed. Like the slices imaged in Figs. 2 and 3, long segments of the graft boundary were adjacent to non-myocyte tissue. In the case of Fig. 4, this buffer consisted of nearly the entire perimeter of the graft—about 800 μ m long—with only one or two sites where host and graft myocytes appeared to be directly adjacent (Fig. 4D[IV]). However, we did not observe any CX43 bridging the host and graft (Fig. 4D[III, IV]).

The lack of CX43 expression between host and graft myocytes likely underlies our functional data (Fig. 4B, C) that show a lack of electrical coupling in either direction between graft and host.

Triggered activity

The 10 myocardial slices that had electrically coupled spheroids were challenged with remote bipolar pacing at rates from 0.5 Hz to 4 Hz in an

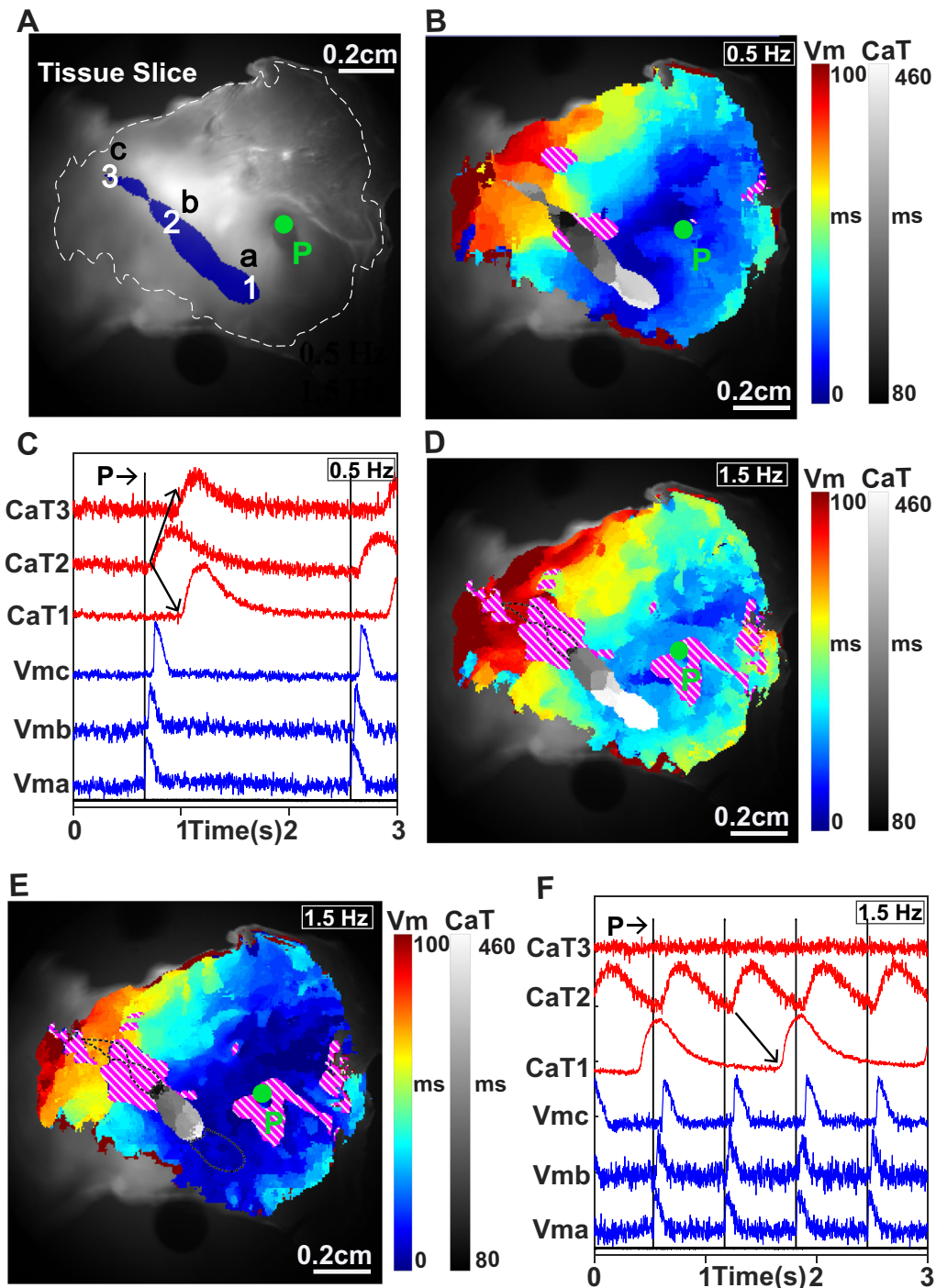


Fig. 1 | Electrical activation in the tissue slice with a large, elongated graft. **A** A representative fluorescence image of the tissue slice with the mapped regions in **(B, D, E)** outlined by a dashed line. Electrically active graft tissue (blue shading) was identified by the presence of CaT signal during electric field pacing. The slice was paced remotely from the graft at site *P*. Vm signals from sites *a, b, c* and CaT signals from sites *1, 2, 3* are shown in **(C, F)**. **B** Activation map in response to 0.5 Hz remote pacing. Vm activation times in the host tissue are rendered in color (blue to red). CaT activation times in the graft are rendered in grayscale (black to white). Regions with poor Vm signal are marked with purple hatching. Activation entered the graft near site 2 and propagated towards sites 1 and 3. **C**, Example CaT signals from sites 1, 2 and 3 in the graft and Vm signals from nearby host myocardial sites *a, b* and *c* during

0.5 Hz remote pacing (vertical lines). Graft site 2 activated first, with propagation continuing to sites 1 and 3 (arrows). **D, E** Vm and CaT activation maps of successive beats in response to 1.5 Hz remote pacing. The color scales and purple hatching are the same as in **(B)**. Activation entered the graft near site 2 similarly to **(B)**. On both beats, activation failed toward site 3. In **(D)** activation propagated all the way to site 1. On the following beat **(E)**, propagation failed part of the way to site 1. Dashed lines show unactivated parts of the graft. **F** Example CaT signals from sites 1, 2 and 3 in the graft and Vm signals from nearby host myocardial sites *a, b* and *c* during 1.5 Hz remote pacing (vertical lines). Activation entered the graft near site 2. Propagation never succeeded toward site 3. Propagation succeeded towards site 1 (arrow) only on every other beat.

attempt to elicit triggered activity. Figure 5A shows Vm and CaT signals recorded during rapid 4 Hz pacing of the slice shown in Fig. 3. Both the host myocardium and graft captured 1:1. Diastolic calcium level in the graft gradually increased, reaching a new steady-state within ~8 pacing cycles (Fig. 5A, CaT). We did not observe delayed afterdepolarizations (DAD) following the rapid pacing trains of 40 cycles (Fig. 5B, CaT) in any of the

slices. Furthermore, during low pacing rates down to 0.5 Hz, we did not observe early afterdepolarizations (EAD) either. It is possible that triggered activity in graft was suppressed due to electrical coupling with surrounding myocardium¹⁵. Thus, in a set of separate experiments, we repeated the same electrical pacing protocol in the isolated, CM-fibroblast spheroids (~600–800 μm diameter). We did not observe either EADs or DADs in this tissue model (Fig. 5C, D).

Table 1 | Transmembrane potential parameters at different pacing rates in the slice shown in Figs. 1 and 2 (α: ratio of propagation velocity in graft compared to host tissue, APD: action potential duration in host tissue, λ: wavelength in host tissue; λ = propagation velocity × APD)

Pacing Rate (Hz)	Propagation Velocity in Host (mm/s)	Propagation Velocity in Graft (mm/s)	α	APD in Host (ms)	λ in Host (mm)
0.5	69.06	19.35	0.28	145.25	10.03
1	65.64	19.22	0.29	136.44	8.95
1.5	53.27	14.54	0.27	131.5	7.00
2	69.65	15.56	0.22	126.75	8.82

Discussion

Remuscularization of damaged myocardium using hiPSC-derived tissue grafts has shown promising therapeutic effects, including improved cardiac function, reduced scar size, and reduced chamber wall stress³. However, arrhythmias associated with the engrafted tissue (EAs) are a long-standing safety concern for translating such therapies to clinical applications. EAs are not typically observed in small animal models (mice, rats, and guinea pigs)¹⁶, likely due to their smaller heart size and higher heart rate. However, they are frequently reported in clinically-relevant large animal models (pigs^{17,18} and nonhuman primates^{10,11,19}).

The mechanisms of EA are poorly understood. Several mechanisms, such as reentry related to conduction heterogeneity, graft automaticity and triggered activity, have been speculated²⁰. In recent studies in pig and

Fig. 2 | Immunohistological imaging of the large, elongated graft implanted by parallel injection. A DAPI staining (blue) and human-specific KU80 labeling (red) indicates human myocytes in the graft. B The addition of α-SA labeling (cyan) indicates cardiomyocytes in both graft and host. The demarcation between the implanted human cardiomyocytes and host myocardium (dotted line) is evident. C, The adjacent serial cryosection with DAPI staining, CX43 labeling (red), and α-SA labeling (cyan). The demarcation between host and graft is still evident. D Magnified view of (C) showing DAPI and CX43. E Magnified view of (C) showing CX43 and α-SA. F Magnified view of C showing DAPI, CX43, and α-SA. CX43 is bridging the host and the graft (arrow) as shown in (D–F). α-SA, α-sarcomeric actin; CX43, connexin-43; and DAPI, 4',6-diamidino-2-phenylindole.

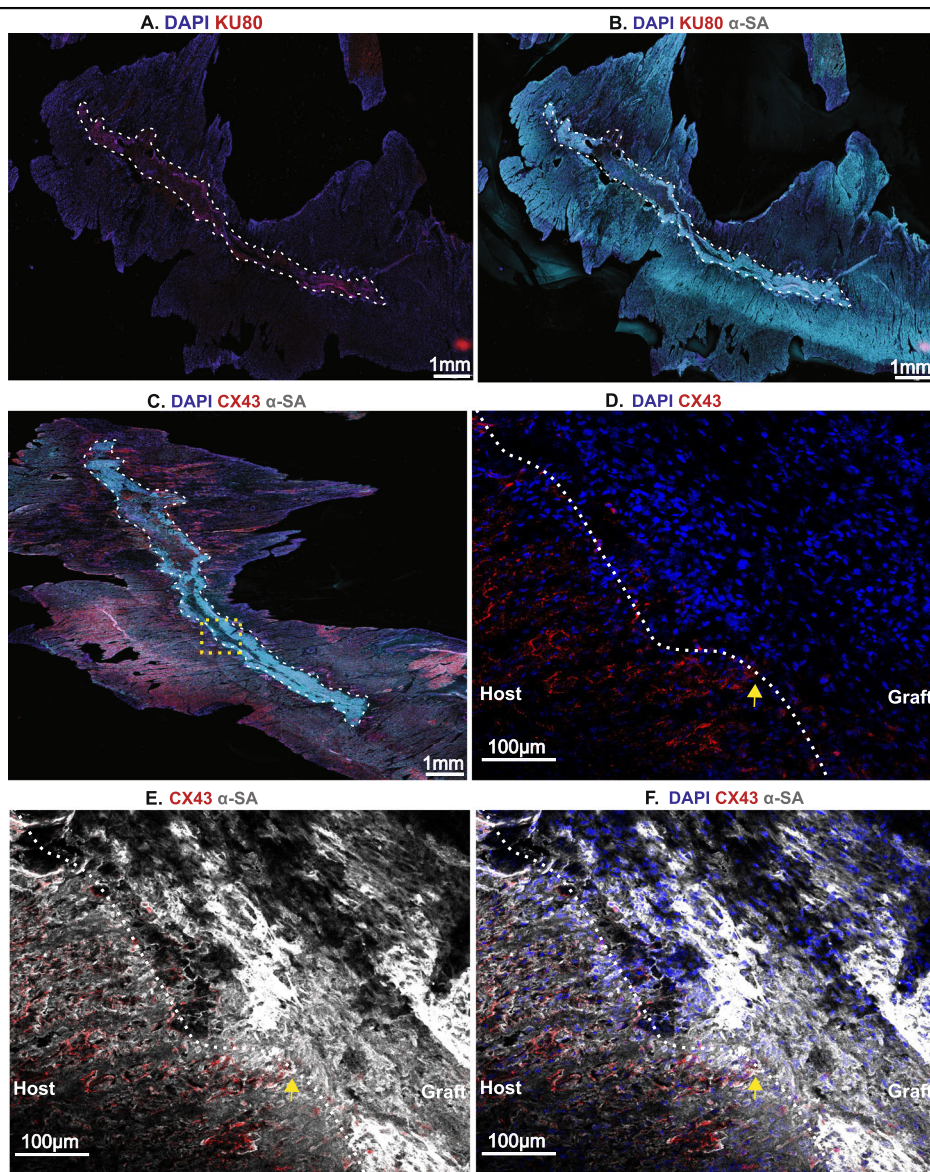
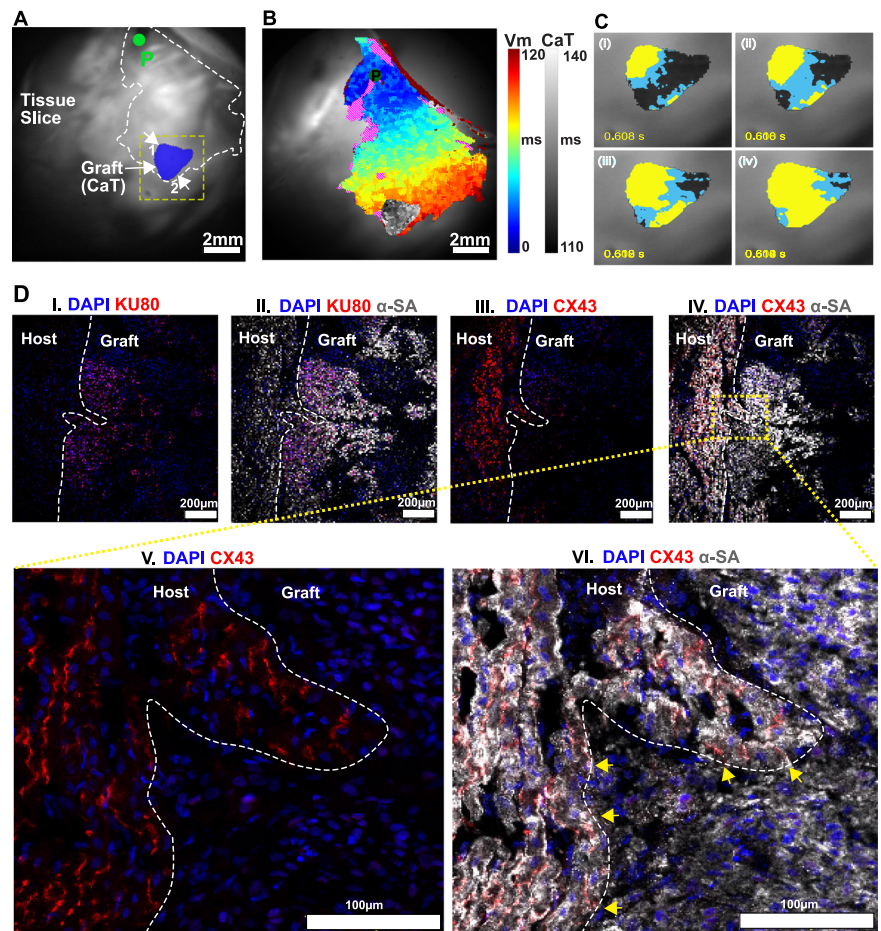


Fig. 3 | Electrical coupling between host and graft at two sites. **A** A representative fluorescence image of a tissue slice with the mapped region in **(B)** outlined by a white dashed line. The blue-shaded region is a tissue graft; the dashed yellow box indicates the region shown in **(C)**. The remote pacing site *P* and the sites where activation entered the graft (*I* and *2*) are indicated (arrows). **B** Activation maps in the host tissue (Vm, color) and graft (CaT, grayscale) during 1 Hz remote pacing. Regions with poor Vm signal are marked with purple hatching. **C** Close-up of graft activation during the beat shown in **(B)**. Pixels above 25% of the maximum CaT deflection are yellow and those in the range 20%–25% are blue. Waves enter at the two sites indicated in **(A)**, merge and propagate to the left and right. Immunostaining of this tissue slice is shown in **(D)**. **D(I)**, A DAPI-stained (blue) cryosection with human-specific KU80 labeling (red). **D(II)**, Additional α -SA labeling (cyan) for cardiomyocytes. The dotted line shows the demarcation between graft and host. **D(III)**, The same section after de-staining and re-staining with DAPI and antibodies for CX43 (red), which indicates structural integration, and in **D(IV)** α -SA (cyan). **D(V)** and **D(VI)** are a magnified view of **D(IV)** showing CX43 bridging the host and the graft (arrows). Vm indicates transmembrane potential; CaT, calcium transients; α -SA, α -sarcomeric actin; CX43, connexin-43; and DAPI, 4',6-diamidino-2-phenylindole.



nonhuman primate models, EA events were electrically mapped using catheter-based methods^{9,11,17}. In those studies, the EAs appeared to be focal in nature and graft automaticity appeared to be the major cause^{9,11,17}. However, the spatial resolution of catheter-based electrical mapping (~1 cm) was insufficient to reveal reentry circuits of smaller size. High resolution optical mapping (~180 μ m) has also been employed to study host-graft coupling in ex vivo whole-hearts from small animals (guinea pigs)^{21,22}. These experiments found potentially arrhythmic properties such as slow conduction, incomplete coupling, and beat-to-beat changes in conduction patterns.

In our previous brief report⁸, we used optical mapping of living myocardial slices harvested from pig hearts 1 week after spheroid implantation to show that the engrafted, tissue was electrically active and coupled with the native myocardium. This was, to our knowledge, the first high-resolution (~50 μ m) imaging of electrical propagation across the graft-host interface. In the present study, we examine that dataset in greater detail. Our *major findings* are that although hiPSC-CM grafts can electrically couple with the host myocardium, the electrical coupling is spatially sparse, with bridges between host and graft on the order of millimeters apart. Furthermore, propagation velocity in the graft is 3-to-5-fold slower than propagation velocity in the host myocardium. These factors reveal potential for the formation of anatomic reentrant circuits. We were unable to induce triggered activity in the grafts, but did directly observe automaticity of engrafted tissue. Notably, we never observed propagation from the graft back into the host tissue and the grafts were therefore not involved in arrhythmic propagation. We did not pace the grafts independently because pacing the grafts with electrical stimuli would also activate underlying and surrounding host tissue. We could therefore not confirm that graft-to-host propagation is possible. However, if grafts can indeed drive host tissue, our observations suggest there is potential for both reentrant and focal graft-associated

arrhythmias. We have recently developed an optogenetic method that will allow us to address this issue in future studies²³. These observations give insight into the mechanisms of engraftment-associated arrhythmias at the 1-week post-implantation timepoint in a clinically-relevant large animal model. They provide important electrical safety information for the design of future cardiac regeneration therapies for ischemic heart disease and reinforce the need for careful arrhythmia management.

We investigated engraftment at one week post-implant because arrhythmia risk is high during the early weeks of transplantation^{10,19}. However, assessing multiple time points^{16,22} or comparing coupling in different injury settings²¹ as other studies have done would provide a more comprehensive understanding of the integration process and associated arrhythmia risks. Furthermore, we implanted the grafts at the time of cardiac injury. Implanting several weeks post-infarct could be a more accurate model of clinical practice.

Electrical coupling between implanted graft and host heart has been observed in both small (mice, rats, and guinea pigs)¹⁶, and large (pigs^{17,18} and nonhuman primates^{10,11,19}) animal models, but the quality of such coupling varies. In our previous brief report on coupling between engrafted hiPSC-CM spheroids and slices of swine myocardium, we found variable coupling, with no coupling at some graft sites ranging to coupling able to sustain 1:1 even with 4 Hz pacing⁸. In the present study, we found that at the 1-week post-implantation timepoint, host-graft electrical coupling occurred at sparsely-distributed discrete bridges. Separation between these bridges was on the order of millimeters. Immunohistology and H&E staining (Figs. 2–4 and Supplementary Figs. S2, S3, S4) suggest that the conduction barriers between bridges were likely caused by the deposition of non-conductive scar tissue around the graft and the lack of gap junctions, which is consistent with previous observations in rodents^{24–26}, pigs⁹, and nonhuman primates¹¹. It is possible that the use of

Fig. 4 | Graft automaticity. **A** Fluorescence image of a slice with a small circular graft (blue circle) that was implanted with perpendicular injection. The remote pacing site (P) and the site of Vm recordings in **(B, C)** are indicated. **B** In the absence of pacing, the graft activated spontaneously at ~0.75 Hz (CaT), but activation did not spread to the host (Vm). **C** During remote pacing, the host activated (Vm), but activation did not spread to the graft (CaT). **D(I)**, Immunohistological image with DAPI staining (blue) and human-specific KU80 labeling (red), which indicates human myocytes in the graft. **(II)**, The same section with additional α -SA labeling (cyan) for cardiac myocytes. The circular demarcation between the implanted human cardiomyocytes and host myocardium (dotted line) is evident in both images. **(III)**, The same section after de-staining and re-staining with DAPI and antibodies for CX43 (red), and in **(IV)**, α -SA. The demarcation between host and graft is still evident. α -SA indicates α -sarcomeric actin; CX43, connexin-43; and DAPI, 4',6-diamidino-2-phenylindole.

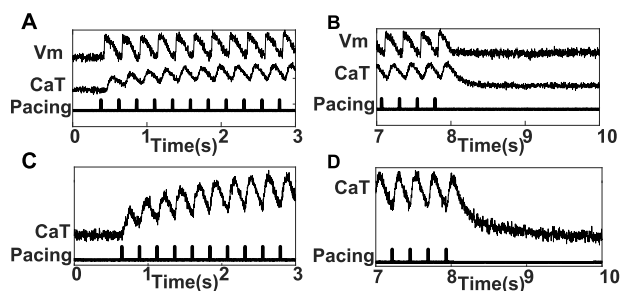
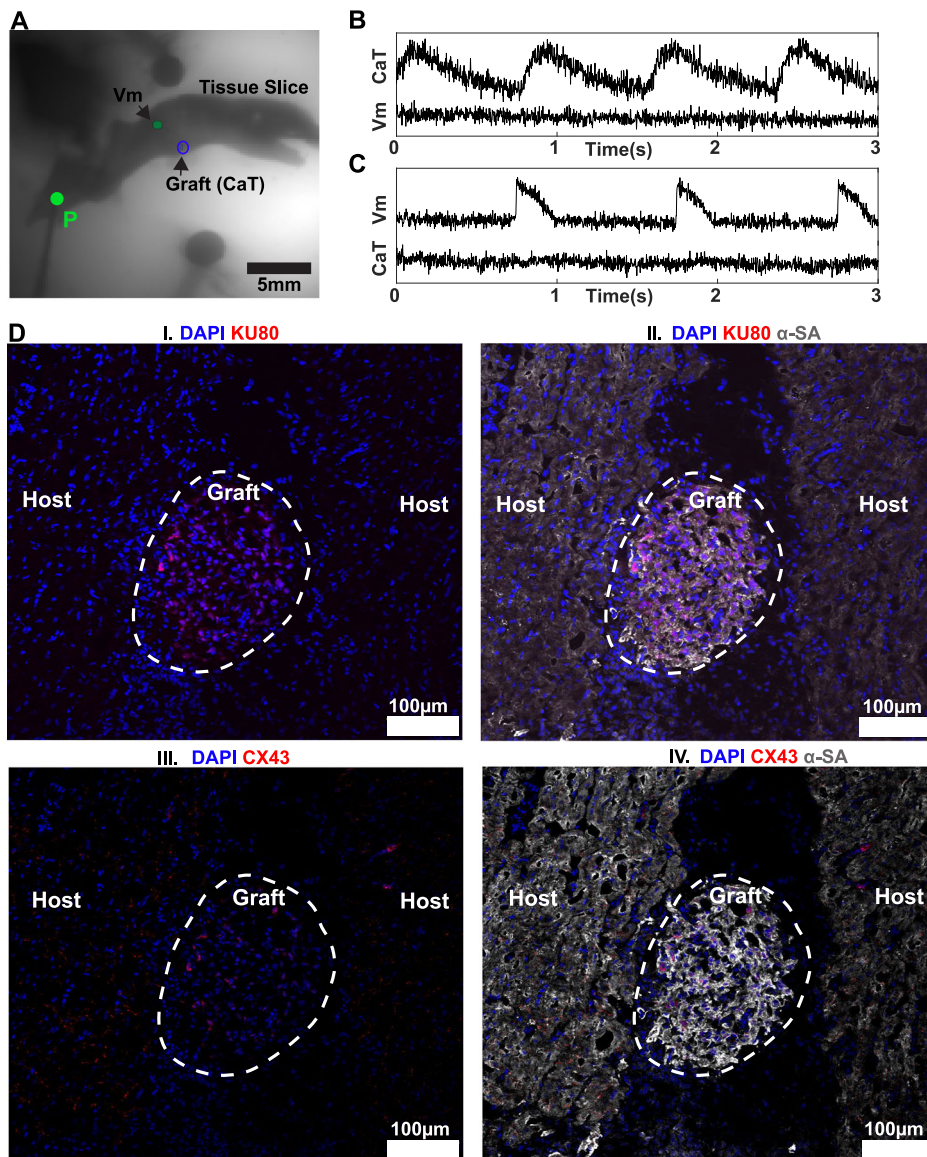


Fig. 5 | Rapid pacing challenge (4 Hz) of the slice shown in Fig. 4 (A, B) and an isolated in vitro spheroid (C, D). **A** Both the graft and the surrounding host myocardium captured the pacing stimuli 1:1. Diastolic calcium level rose for about 2 s, then reached a new steady state. **B** Following the end of rapid pacing train (10 s; 40 cycles) no delayed afterdepolarization was observed in the graft. **C** CaT signal from an isolated CM-fibroblast spheroid 600–800 μ m in diameter during 4 Hz pacing. The spheroid captured 1:1. The diastolic calcium level gradually increased but reached steady state after ~2 s. **D** Following the end of the pacing train (10 s; 40 cycles), delayed afterdepolarization (DAD) was not observed.

paraffin embedding²⁷ rather than cryo-sectioning in creating the immunohistological images could have revealed greater detail on tissue structure in these regions. Heterotypic electrical coupling between myocyte and non-myocyte is possible²⁸, but the electrical coupling in non-myocytes is too weak to maintain passive electrical propagation over long distance²⁹. Another factor is that myocyte orientation in the graft tissue was not controlled during either fabrication or implant. The resulting misalignment between host and graft myocytes may be unfavorable for establishing reliable electrical coupling across the host-graft interface (Fig. 2 and Supplementary Figs. S2, S3). Even in the host-graft bridges shown in Figs. 2, 3, and Supplementary Fig. S4, there was an abrupt change in cardiomyocyte orientation at the interface. In some cases, transitioning from a region with high conductivity (e.g., longitudinal fiber orientation) to low conductivity (e.g., transverse fiber orientation) may enhance propagation reliability³⁰. However, studies in patterned engineered tissue³¹ as well as whole mammalian hearts^{32,33} have shown that regions with abrupt changes in fiber orientation are prone to propagation delay and failure.

Slow speed and conduction failure were key features of electrical propagation within the grafts. In the elongated graft that resulted from parallel injection, propagation was 3-5 times slower than in the host tissue

(Table 1). This might have been ameliorated by using grafts fabricated from multiple cell types. For example, we previously showed that in tissue patches made from four types of hiPSC-derived cells, conduction velocity measured in vitro approached that of in situ myocardium³⁴. We also observed rate-dependent conduction block between the site at which activation entered the graft (site 2) and the two ends of the graft (sites 1 and 2; Fig. 1, Supplementary Fig. S1 and Supplementary Movies 1–4). This likely resulted at least partly from low CX43 expression in the graft, which was evident in our immunohistological imaging (Fig. 2 and Fig. S2) and is a known feature of stem-cell-derived cardiomyocytes³⁵. Other factors that may have contributed to poor in-graft conduction include the shock of initial cross-species transplantation from cell culture conditions to the harsh environment of the ischemic border zone, and other immaturities of stem-cell-derived cardiomyocytes, such as low excitability due to immature sodium channel expression and distribution, lack of t-tubule structure, etc³⁵.

Anatomic reentry is an abnormal mode of propagation in which electrical waves circulate about an inexcitable barrier³⁶. While we did not observe reentry in our experiments, there was potential for it to form. The millimeter-scale distance between graft-host bridges creates anatomic barriers about which reentry can circulate. Furthermore, the slow/unreliable conduction within grafts that we observed creates circumstances for reentry initiation. One potential mechanism is revealed by Fig. 1 and Supplementary Movie 1. Conduction entered the graft at site 2 then propagated slowly (in the opposite direction as the host wave) back to site 1. When the wave reached site 1, sufficient time had elapsed for the surrounding host tissue to repolarize. Had there been an additional host-graft bridge at site 1 that supported graft-to-host propagation, a reentrant circuit cycling from host-to-graft-to-host-to-graft could be formed. Let L be the distance between two graft-host bridges (e.g., at site 2 and the putative one at site 1), V the propagation velocity in the host tissue, αV the propagation velocity in the graft (where $\alpha < 1$), and APD the action potential duration in the host tissue. The time to conduct between the two sites in the host tissue is L/V , and between the two sites in the graft, $L/\alpha V$. Therefore, reentry by this mechanism is possible if

$$\frac{L}{V} + \frac{L}{\alpha V} > APD \quad (1)$$

Equation (1) assumes that APD is a valid approximation of the refractory period, which is normally the case except in situations such as acute ischemia that induce postrepolarization refractoriness¹³. The conduction wavelength in the host tissue (i.e., the distance between the depolarizing wavefront and the repolarizing wave tail) is defined as $\lambda = V \cdot APD$. Substituting into (1), the condition for reentry becomes

$$L > \frac{\lambda}{(1 + \frac{1}{\alpha})} \quad (2)$$

In our data, at 2 Hz, the right-hand-side of (2) is ~2 mm (refer to Table 1). Reentry is therefore possible not only in the elongated graft of Fig. 1, but in the much smaller graft of Fig. 3.

It is worth noting that in the slice with the elongated graft, the wave propagating through the host tissue from the pacing site reached site 1 before site 2. Therefore, for retrograde propagation from site 2 to 1 in the graft to be established, on at least one pacing cycle, there would have to be unidirectional conduction block on entry at site 1 or between site 1 and site 2. This could result from a mismatch in refractory period in the host and graft tissue or from failed conduction in the graft (such as in Fig. 1E).

The large difference in conduction velocity between graft and host suggests a second potential mechanism for reentry to be established. In the slice in Fig. 1, suppose activation from the host entered the graft at site 1. If the wave in the host tissue reached site b (opposite site 2) and blocked on entry to the graft, and in addition, the host tissue had time to recover before the wave in the graft reached site 2, the graft wave could have re-entered the

host at site b and initiated a reentrant circuit. Quantitatively, the condition for this to occur is

$$\frac{L}{V} + APD < \frac{L}{\alpha V} \quad (3)$$

Solving for L and substituting the definition for wavelength, we obtain

$$L > \frac{\lambda}{(\frac{1}{\alpha} - 1)} \quad (4)$$

as the condition for reentry. In our data, with 2 Hz pacing, the right-hand-side of (4) is ~3 mm (refer to Table 1). This reentry mechanism requires a larger distance between graft-host bridges than the mechanism in (2). The graft in Fig. 3, with ~2 mm between bridges is too small for this mechanism, but had there been a second graft-host bridge at site 1 in the graft of Fig. 1, reentry induction by this mechanism would have been possible.

This analysis suggests that for safety from reentry by either mechanism, tissue grafts should be in small islands less than 2–3 mm in size. It is worth noting that in previous studies that reported engraftment arrhythmias, tissue grafts were typically several millimeters along their longest dimension^{10,11,16,17}. Larger values of α , due either to graft maturation or improved graft engineering technology, would increase the bridge-bridge distance L required for reentry and allow larger islands. In addition, the potential for anatomic reentry by either mechanism is likely to decrease as the graft-host interface matures. Coupling with the host is expected to strengthen with maturation^{10,11,37}, and the bridge-bridge distance could therefore decrease below the values of L that favor reentry induction.

Spontaneous activation of a graft may serve as an ectopic focus to initiate an EA. Spontaneous activation could potentially arise from graft automaticity or triggered activity. Graft automaticity has been a long-standing safety concern for cardiac cell therapy because automaticity is one of the common features of hiPSC-CMs. In the present study, automaticity was observed, but only in one slice (Fig. 4). It is worth noting that our myocardial slices were treated with BDM for optical mapping. In our pilot studies, BDM suppressed spontaneous activation of hiPSC-CMs in vitro. We and others have observed that BDM can suppress spontaneous activation in whole hearts^{38,39}. In iPSC-derived cardiomyocytes, automaticity is thought to be regulated by sarcoplasmic reticulum calcium release⁴⁰ and BDM is known to reduce intracellular calcium release⁴¹; thus, we believe the prevalence of graft automaticity could be underestimated in the present study.

Triggered activity, i.e., the premature activation by early or delayed afterdepolarizations (EAD/DAD), is another common mechanism underlying arrhythmia onset. EADs and DADs involve complex interactions among various ionic currents and intracellular calcium handling processes. DADs occur in diastole when calcium is spontaneously released from the sarcoplasmic reticulum (SR). This activates the sodium-calcium exchanger (NCX), which may admit enough depolarizing current to elicit a full triggered beat. DADs occur under conditions of calcium overload and are facilitated by rapid heart rate. EADs occur during repolarization under conditions that prolong the action potential. They may be driven by L-type calcium channels recovering from inactivation or by spontaneous calcium release from the SR that triggers NCX. They are facilitated by slow heart rates⁴². In the present study, neither the transplanted grafts nor isolated spheroids exhibited EADs or DADs during activation rates ranging from to 0.5 Hz to 4 Hz. This suggests our hiPSC-CMs were resistant to afterdepolarizations across a wide range of pacing rates from slow (0.5 Hz), which might facilitate EADs, to fast (4 Hz), which might facilitate DADs. However, we did not challenge the engineered tissue with pathological conditions such as hypoxia, hypokalemia etc. that might promote triggered activity. Ideally, for the safety of the cardiac cell therapy, transplanted grafts should not be more sensitive to adverse conditions than the native myocardium.

For a spontaneous beat in a graft to become a full-blown ectopic activation of the heart, there must be sufficient coupling for the electrical

wave emerging from the graft to overcome the electrical load of the host myocardium and initiate a propagating wave in the host^{15,43}. We never observed waves leaving a graft and entering the host, so it is possible that at this time point post-implantation, the unorganized and relatively poorly coupled CMs in the graft were unable to produce sufficient depolarizing current to drive the host tissue through the sparse graft-host bridges. In particular, the graft shown in Fig. 5, which exhibited spontaneous activity, never drove the surrounding host tissue. However, as implanted grafts mature in vivo, electrical coupling is expected to strengthen over time^{10,11,37}, possibly eventually favoring ectopy. On the other hand, very strong graft-host coupling could suppress spontaneous beats in the graft by draining away and dissipating depolarizing current into the large sink of the host myocardium. This would be more likely with small grafts^{15,43}. It is therefore possible that the potential for ectopy is biphasic, with low potential early and late after implant, with higher potential at intermediate times. If this is the case, the present study reflects the early, low-potential period.

Methods

All animal experimental protocols were approved by Institutional Animal Care and Use Committee (APN 21498) at University of Alabama at Birmingham (UAB) and were in accordance with the Guide for the Care and Use of Laboratory Animals. All cells used in the study were differentiated from human induced pluripotent stem cell (hiPSC) line LZ-hiPSC5 which was reprogrammed from human cardiac fibroblasts⁴⁴. The hiPSCs were expanded and maintained as described previously^{3,44}.

hiPSC-CM Spheroid Preparation

We differentiated hiPSCs into hiPSC-CMs via the GiWi method⁴⁵. We adapted a previously developed bioreactor suspension 3D culture protocol to produce hiPSC-CM spheroids at large scale with high purity⁴⁶. Briefly, hiPSCs were cultured in a 125 mL Erlenmeyer flask on an orbital shaker (The Belly Dancer, MilliporeSigma) for 4 days with TeSR-E8 3D Seed medium (#03990, STEMCELL Technologies). On Day 0, differentiation was initiated by replacing culture medium with RPMI 1640 (#11875093, Gibco) supplemented with B27 without insulin (RPMI/B27-; #A1895601, Gibco) and 6 μM CHIR99021 (#72054, STEMCELL Technologies). On Day 1, the medium was replaced with fresh RPMI/B27- and 1 μM CHIR99021. On Day 3, 70% of the culture medium was replaced with fresh RPMI/B27- with a final concentration of 5 μM IWR-1-endo (#72562, STEMCELL Technologies). On Day 5, the medium was replaced with fresh RPMI/B27-. On Day 7, the medium was changed to RPMI supplemented with B27 with insulin (RPMI/B27 +; #A3582801, Gibco). On Day 9, the spheroids were purified via metabolic selection following a previously described protocol^{46,47}. On Day 12, we obtained spontaneously beating hiPSC-CM spheroids of 200–250 μm in diameter. Each hiPSC-CM spheroid consisted of ~4000 CMs counted via trypan blue staining after dissociation of spheroids into single myocytes. Each batch contained ~50 million CMs with purity >90% (cardiac Troponin T positive by

flowcytometry). After purification, the hiPSC-CM spheroids were maintained in RPMI/B27+.

We also prepared larger spheroids for mapping in vitro without implantation into pig hearts. We mixed hiPSC-CM spheroids with cardiac fibroblasts (also differentiated from the LZ-hiPSC5 cell line) in a 4:1 cell ratio and cultured for an additional week. This resulted in larger spontaneously beating cardiac spheroids. Each was 600–800 μm in diameter and contained 100 × 10³ cardiac myocytes and 25 × 10³ cardiac fibroblasts²³. After fabrication, they were maintained in the same manner as the hiPSC-CM spheroids.

Lentiviral Transduction of GCaMP6

The hiPSC-CM spheroids were transduced with GCaMP6, a green GECL, using a lentiviral vector. Lentivirus encoding MHCK7-GCaMP6 was produced following a previously published protocol⁴⁸. Briefly, the plasmid pRRL-MHCK7-GCaMP6 (#65042, Addgene) was obtained and transfected to HEK 293 T cells along with the envelope plasmid pMD2.G (#12259, Addgene) and the packaging plasmid psPAX2 (#12260, Addgene). The viral particles were collected, purified, and concentrated on Day 2 and Day 4. The viral pellets were resuspended, and the viral stocks were stored at -80 °C.

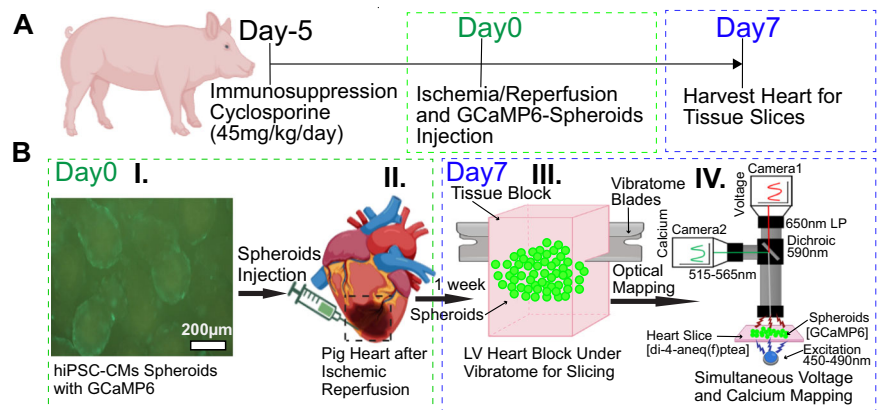
The transduction was carried out by adding the lentiviral vectors to the hiPSC-CM spheroid culture 5 days before the spheroid transplantation. The expression of GCaMP6 in hiPSC-CMs was driven by the muscle-specific promoter MHCK7²⁵. The functional expression of GCaMP6 was typically visible (as green fluorescence flashing at every contraction) under a fluorescence microscope (CKX53, Olympus) 3 days after transduction, at which time the lentiviral particles were removed from the hiPSC-CM spheroid culture with a medium change.

Porcine ischemia/reperfusion model and hiPSC-CM Spheroid transplantation

Acute Myocardial Infarction (AMI) was induced in anesthetized juvenile Yorkshire cross pigs (*n* = 6; 3 males and 3 females; 10-25 kg, Valley Brook Research, GA) following an established ischemia/reperfusion (I/R) protocol⁴⁹. Our previous brief report included data from these animals. Briefly, anesthesia was induced with intramuscular telazol/xylazine (4.4 mg/kg, 4.4 mg/kg, respectively) and maintained with isoflurane by inhalation in 100% oxygen (1.5–2.5%). The chest was opened via median sternotomy to expose the heart. AMI was created by balloon occlusion of the left anterior descending coronary artery (LAD) distal to the 2nd diagonal branch for 1 h followed by reperfusion and anticoagulation.

GCaMP6-expressing hiPSC-CM spheroids containing a total of 50 million hiPSC-CMs were transplanted to the AMI border zone immediately after the I/R procedure (Fig. 1A). Before transplantation, spheroids were washed using DPBS (#14190235, Gibco) to remove any remaining viral vectors, and then resuspended in 1 mL RPMI without B27 supplements (Fig. 6B[I]). The spheroid suspension was injected into 4 sites (0.25 mL spheroids suspension each) within the left ventricular AMI border zone using a 20 Gauge hypodermic needle (Fig. 6B[II]). The needle was slowly

Fig. 6 | Study protocol. **A** Pigs were immunosuppressed for 5 days before infarct creation by ischemia/reperfusion and GCaMP6-spheroid injection. Heart harvest was 7 days after the implantation. **B** Cardiac spheroids (200–250 μm in diameter) transduced with GCaMP6 were implanted into the immunosuppressed pig’s heart on Day 0 (I and II) and the heart was harvested for tissue slicing and imaging on Day 7 (III and IV). Created with BioRender.com.



withdrawn during injection, leaving a column filled with spheroid suspension (Fig. 6B[III]). In one animal, the needle tracks were nearly parallel to the epicardial surface (*parallel injection*) to maximize the graft size in tissue slices, which were taken parallel to the epicardium. In the other 5 animals, the needle tracks were nearly perpendicular to the epicardial surface, to maximize the number of graft-containing tissue slices (*perpendicular injection*). After each injection, a suture was placed on the injection site to mark the location.

The pigs were immunosuppressed to protect the transplanted grafts from rejection. Cyclosporine A was administered twice daily starting 5 days before the spheroid transplantation procedure (15 mg/kg in the morning and 30 mg/kg in the evening; Novartis). Abatacept (12.5 mg/kg; Bristol-Myers Squibb) was administered once on the day of surgery. Post-surgery, methylprednisolone was administered daily until the terminal study (250 mg on the day of I/R procedure and 1.5 mg/kg/day afterward; Pfizer)⁵⁰.

Heart Harvesting and Tissue Slice Preparation

On post-transplantation Day 7, the hearts were harvested with a second open-chest surgery. Animal preparation and anesthesia were similar to those in the previous procedure. Heart excision and cannulation were similar to our previous publication⁵¹. Briefly, the heart was rapidly excised and placed in a bath of ice cold 0.9% saline (IM-4390, ICU Medical Inc.). The aortic root was cannulated and coronary arteries were flushed with 1 L chilled (0 °C) cardioplegic solution (110 mM NaCl, 1.2 mM Ca₂Cl₂, 16 mM KCl, 16 mM MgCl₂, 10 mM NaHCO₃, 7.4 pH). Euthanasia was by exsanguination secondary to heart excision.

Transmural tissue blocks approximately 1.5 cm by 1.5 cm were excised from the region surrounding each spheroid injection site. The tissue blocks were immersed in oxygenated, ice-cold modified Tyrode's solution (140 mM NaCl, 6 mM KCl, 10 mM glucose, 10 mM HEPES, 1 mM MgCl₂, 1.8 mM CaCl₂, 7.4 pH) supplemented with 2,3-butanedione monoxime (BDM, 20 mM; #B0753, Sigma-Aldrich) while waiting for tissue slicing. BDM is known to have cardioprotective effects⁵².

Our living myocardial slice protocol was similar to a previous publication⁵³. Briefly, the tissue blocks were mounted to a high-precision vibratome (7000smz-2, Campden Instruments Ltd. UK) with the epicardium facing downward and were fully immersed in oxygenated, ice-cold modified Tyrode's solution supplemented with BDM (the same composition as described above). The tissue blocks were sliced parallel to the epicardium with thickness 600 μm, 0.03 mm/s advance speed, 2 mm horizontal vibration amplitude, and 80 Hz vibration frequency (Fig. 6B[III]). The vibratome's z-axis vibration was calibrated prior to each experiment with a ceramic cutting blade and set to <0.5 μm. After slicing, the myocardial slices were maintained in oxygenated, room temperature, modified Tyrode's solution for a minimum of 20 min before mapping to allow recovery. BDM (20 mM) was added to recovery solution for its cardioprotective effects and to prevent slice curling.

Simultaneous voltage and calcium mapping

A custom-built membrane potential (Vm) and calcium transient (CaT) dual-parametric optical mapping system was used to image the electrical activity in the myocardial slices⁸. The myocardial slices were stained with a VSD (di-4-ANEQ[F]PTEA, Potentiometric Probes) and maintained in oxygenated, 37 °C, modified Tyrode's solution supplemented with BDM (same composition as above). A bandpass filtered (425–490 nm; FF01-460/60-25, Semrock), high-power blue LED light source (LIC1-BLU1000000000, Lumileds) was used to excite both GECI and VSD simultaneously. The emitted fluorescence was split by a dichroic beam splitter (cut-off: 590 nm; #66-251, Edmund Optics) into CaT and Vm channels. The CaT channel was further bandpass filtered at 515–565 nm (#447744-8001, Zeiss) and the Vm channel was further longpass filtered above 650 nm (#62986, Edmund Optics). The CaT and Vm channels were simultaneously recorded with a pair of synchronized cameras (MiCAM03-N256, SciMedia) at 500 fps (Fig. 6B[IV]). Because only transplanted hiPSC-CMs spheroids express GCaMP6, the CaT signal is a tissue-specific

surrogate for electrical activity in the grafts. The VSD stains all tissue, so Vm signals represent the overall electrical activity in the myocardial slices.

Experimental protocol

Tissue slices were placed in the optical mapping system and pinned to the bottom of the chamber. Each slice was stimulated with electric field pacing in a similar manner to previous studies⁵⁴ to screen for the presence of electrically active spheroids. The electrode plates were positioned at opposite ends of the mapping chamber and did not contact the tissue itself. Field pacing stimulates all cells in the tissue slice simultaneously, regardless of intracellular electrical coupling. Because only hiPSC-CM grafts expressed GCaMP6, the presence of CaT signal (which we defined as signal-to-noise ratio >5) indicated the presence and the location of surviving grafts. The stimulus strength was ~15 V/cm, which was large enough to reliably activate slices. Although this stimulus is in the defibrillation range with potential for tissue damage, we did not observe such damage, possibly because the majority of the stimulus current was shunted through the bath fluid.

Slices containing electrically active grafts that were identified by field pacing were then paced using a pair of closely spaced bipolar electrodes positioned in the host myocardium remotely from the graft. The remote bipolar pacing rate varied from 0.5 to 4 Hz. The pacing strength was set to twice diastolic threshold at 0.5 Hz. The slices were also mapped without pacing to examine graft automaticity.

After optical mapping, the myocardial slices containing grafts were cryopreserved in sucrose. The slices were then embedded in optimal cutting temperature compound (OCT; #23-730-571, Fisher Scientific) and 10 μm serial cryosections were obtained for immunohistological and hematoxylin and eosin (H&E) staining.

Signal Processing

To produce activation maps, Vm and CaT signals were processed with an 11-point median filter and then with an 11-point, third order Savitsky-Golay first-derivative filter⁵⁵. Positive peaks in the first-derivative signal (i.e., the time of most rapid depolarization) were taken as activation times. Vm signals were visually screened for distorted baselines. Such signals were generally caused by ripples in the bath and occasionally produced anomalous activation times; they were rejected from further analysis. We evaluated the conduction velocity in both the host myocardium and the graft using the method of Bayly et al.⁵⁶ Briefly, activation time maps were fitted to polynomial surfaces, and the conduction velocity was calculated from the gradient of the local polynomial surface. We identified repolarization in the Vm signals by filtering the signals with an 11-point, third order Savitsky-Golay second derivative filter⁵⁵. Positive second derivative peaks reveal the return to baseline and were taken as the repolarization time. Action potential duration (APD) was the interval between depolarization and repolarization⁵⁷. APD was not evaluated in the graft because Vm signals from graft tissue could not be separated from Vm signals generated by surrounding/underlying host tissue.

Immunohistological staining

Immunohistology was used to identify engrafted human cells within the host tissue and the gap junction protein connexin-43 (CX43). The cryosections for immunohistological staining were processed following previously published protocols^{7,58}. In brief, the cryosections were fixed with 4% paraformaldehyde for 20 min at room temperature, permeabilized with 0.1% Triton X-100 (#9036-19-5, Sigma-Aldrich) for 15 min at 4 °C, and then incubated with DPBS containing 10% donkey serum and a 1:100 dilution of primary antibodies overnight at 4 °C. We did not find suitable antibodies to co-stain human nuclei and CX43. Therefore, for slices with small tissue grafts resulting from perpendicular injection, we first stained cryosections with the human-specific nuclear marker KU80 Rabbit IgG (KU80; #2180, Cell Signaling), the myocyte marker alpha-sarcomeric Actin Mouse IgM (α-SA; #A2172, Sigma-Aldrich), and the nuclear marker DAPI (4,6-diamidino-a-phenyl-indole, Sigma-Aldrich). The secondary antibody

for KU80 was TRITC-conjugated donkey anti-rabbit IgG, and for α -SA was Cy5-conjugated donkey anti-mouse IgM (both from Jackson ImmunoResearch Laboratories). After overnight incubation with primary antibodies, the cryosections were stained with secondary antibodies with 1:200 dilutions for 1 h at 4 °C. The stained cryosections were imaged using a confocal microscope (FV3000, Olympus). After imaging, staining was removed by immersing the cryosection in 70% ethyl alcohol for 10 min and then gently removing the cover slide. The cryosection was then immersed in fresh 70% ethyl alcohol for 30 min and washed with DPBS for 5 min three times. The cryosection was re-stained in a similar manner with rabbit IgG anti-CX43 (#AF0137, Affinity), α -SA, and DAPI and imaged again. The secondary antibody for CX43 was TRITC-conjugated donkey anti-rabbit IgG (Jackson ImmunoResearch Laboratories).

For slices with large tissue grafts resulting from parallel injection, we mounted adjacent cryosections from the slice on the same slide. One cryosection was stained as above for KU80, α -SA, and DAPI, while the other was stained for CX43, α -SA, and DAPI. For these large (centimeter-scale) grafts, having tissue with both sets of labels simultaneously available facilitated navigating the sections to identify the host-graft interface and co-located CX43 expression.

Hematoxylin and eosin staining

Cryosections were thawed at room temperature for 5 min and washed in water for another 5 min to remove the OCT. The cryosections were then fixed in Bouin's solution (#HT10132, Sigma-Aldrich) for 30 min. After fixation, cryosections were incubated in Eosin (#22-500-063, Fisher Scientific) for 20 sec, washed three times in water (2 min each time) followed by 5 min incubation in Hematoxylin (#22-500-051, Fisher Scientific) and then washed again three times in water (2 min each time). For dehydration, sections went through a series of changes of ethanol (first: 80% ethanol for 2 min, second: 100% ethanol for 2 min, and third: 100% ethanol for 2 min) and three changes of Xylene for 2 min each. Then, the sections were mounted with mounting media (Toluene; #SP15-100, Fisher Scientific) for imaging.

Data availability

Data will be made available from the corresponding author upon reasonable request.

Received: 14 January 2025; Accepted: 9 September 2025;

Published online: 03 November 2025

References

- Bishop, S. P., Zhang, J. & Ye, L. Cardiomyocyte proliferation from fetal- to adult- and from normal- to hypertrophy and failing hearts. *Biology* **11**. <https://doi.org/10.3390/biology11060880> (2022).
- Ye, L. et al. Early regenerative capacity in the porcine heart. *Circulation* **138**, 2798–2808 (2018).
- Ye, L. et al. Cardiac repair in a porcine model of acute myocardial infarction with human induced pluripotent stem cell-derived cardiovascular cells. *Cell Stem Cell* **15**, 750–761 (2014).
- Zhu, W., Zhao, M., Mattapally, S., Chen, S. & Zhang, J. CCND2 overexpression enhances the regenerative potency of human induced pluripotent stem cell-derived cardiomyocytes: remuscularization of injured ventricle. *Circ. Res.* **122**, 88–96 (2018).
- Sadek, H. & Olson, E. N. Toward the goal of human heart regeneration. *Cell Stem Cell* **26**, 7–16 (2020).
- Zhao, M. et al. Cyclin D2 overexpression enhances the efficacy of human induced pluripotent stem cell-derived cardiomyocytes for myocardial repair in a swine model of myocardial infarction. *Circulation* **144**, 210–228 (2021).
- Tan, S. H. et al. Thymosin beta4 increases cardiac cell proliferation, cell engraftment, and the reparative potency of human induced-pluripotent stem cell-derived cardiomyocytes in a porcine model of acute myocardial infarction. *Theranostics* **11**, 7879–7895 (2021).
- Guragain, B. et al. Implanted human cardiac spheroids electrically couple with infarcted swine myocardium. *Circulation* **149**, 1855–1857 (2024).
- Marchiano, S. et al. Gene editing to prevent ventricular arrhythmias associated with cardiomyocyte cell therapy. *Cell Stem Cell* **30**, 396–414 e399 (2023).
- Kobayashi, H. et al. Regeneration of nonhuman primate hearts with human induced pluripotent stem cell-derived cardiac spheroids. *Circulation* <https://doi.org/10.1161/CIRCULATIONAHA.123.064876> (2024).
- Liu, Y. W. et al. Human embryonic stem cell-derived cardiomyocytes restore function in infarcted hearts of non-human primates. *Nat. Biotechnol.* **36**, 597–605 (2018).
- Biermann, M. et al. Differential effects of cytochalasin D and 2,3 butanedione monoxime on isometric twitch force and transmembrane action potential in isolated ventricular muscle: implications for optical measurements of cardiac repolarization. *J. Cardiovasc. Electrophysiol.* **9**, 1348–1357 (1998).
- Coronel, R., Janse, M. J., Opthof, T., Wilde, A. A. & Taggart, P. Postrepolarization refractoriness in acute ischemia and after antiarrhythmic drug administration: action potential duration is not always an index of the refractory period. *Heart Rhythm* **9**, 977–982 (2012).
- de Bakker, J. M. et al. Reentry as a cause of ventricular tachycardia in patients with chronic ischemic heart disease: electrophysiologic and anatomic correlation. *Circulation* **77**, 589–606 (1988).
- Gibbs, C. E. et al. Graft-host coupling changes can lead to engraftment arrhythmia: a computational study. *J. Physiol.* **601**, 2733–2749 (2023).
- Shiba, Y. et al. Human ES-cell-derived cardiomyocytes electrically couple and suppress arrhythmias in injured hearts. *Nature* **489**, 322–325 (2012).
- Selvakumar, D. et al. Cellular heterogeneity of pluripotent stem cell-derived cardiomyocyte grafts is mechanistically linked to treatable arrhythmias. *Nat. Cardiovasc. Res.* **3** <https://doi.org/10.1038/s44161-023-00419-3> (2024).
- Kawaguchi, S. et al. Intramyocardial transplantation of human iPSC cell-derived cardiac spheroids improves cardiac function in heart failure animals. *JACC Basic Transl. Sci.* **6**, 239–254 (2021).
- Chong, J. J. et al. Human embryonic-stem-cell-derived cardiomyocytes regenerate non-human primate hearts. *Nature* **510**, 273–277 (2014).
- Paci, M., Penttinen, K., Pekkanen-Mattila, M. & Koivumaki, J. T. Arrhythmia mechanisms in human induced pluripotent stem cell-derived cardiomyocytes. *J. Cardiovasc. Pharm.* **77**, 300–316 (2020).
- Filice, D. et al. Optical mapping of human embryonic stem cell-derived cardiomyocyte graft electrical activity in injured hearts. *Stem Cell Res. Ther.* **11**, 417 (2020).
- Dahri, W. et al. In vitro matured human pluripotent stem cell-derived cardiomyocytes form grafts with enhanced structure and function in injured hearts. *Circulation* **145**, 1412–1426 (2022).
- Guragain, B. et al. Optogenetic stimulation and simultaneous optical mapping of membrane potential and calcium transients in human engineered cardiac spheroids. *J. Mol. Cell Cardiol.* **199**, 51–59 (2025).
- Weinberger, F. et al. Cardiac repair in guinea pigs with human engineered heart tissue from induced pluripotent stem cells. *Sci. Transl. Med.* **8**, 363ra148 (2016).
- Jackman, C. P. et al. Engineered cardiac tissue patch maintains structural and electrical properties after epicardial implantation. *Biomaterials* **159**, 48–58 (2018).
- Laflamme, M. A. et al. Cardiomyocytes derived from human embryonic stem cells in pro-survival factors enhance function of infarcted rat hearts. *Nat. Biotechnol.* **25**, 1015–1024 (2007).
- Zhanmu, O., Yang, X., Gong, H. & Li, X. Paraffin-embedding for large volume bio-tissue. *Sci. Rep.* **10**, 12639 (2020).

28. Wang, Y. et al. Fibroblasts in heart scar tissue directly regulate cardiac excitability and arrhythmogenesis. *Science* **381**, 1480–1487 (2023).
29. Gaudesius, G., Miragoli, M., Thomas, S. P. & Rohr, S. Coupling of cardiac electrical activity over extended distances by fibroblasts of cardiac origin. *Circ. Res.* **93**, 421–428 (2003).
30. Boyle, P. M. et al. New insights on the cardiac safety factor: unraveling the relationship between conduction velocity and robustness of propagation. *J. Mol. Cell Cardiol.* **128**, 117–128 (2019).
31. Badie, N., Scull, J. A., Klinger, R. Y., Krol, A. & Bursac, N. Conduction block in micropatterned cardiomyocyte cultures replicating the structure of ventricular cross-sections. *Cardiovasc. Res.* **93**, 263–271 (2012).
32. Bourgeois, E. B., Reeves, H. D., Walcott, G. P. & Rogers, J. M. Panoramic optical mapping shows wavebreak at a consistent anatomical site at the onset of ventricular fibrillation. *Cardiovasc. Res.* **93**, 272–279 (2012).
33. Iijima, K. et al. Right ventricular insertion promotes reinitiation of ventricular fibrillation in defibrillation failure. *Heart Rhythm* **18**, 995–1003 (2021).
34. Lou, X. et al. Cardiac muscle patches containing four types of cardiac cells derived from human pluripotent stem cells improve recovery from cardiac injury in mice. *Cardiovasc. Res.* <https://doi.org/10.1093/cvr/cvad004> (2023).
35. Feinberg, A. W. et al. Functional differences in engineered myocardium from embryonic stem cell-derived versus neonatal cardiomyocytes. *Stem Cell Rep.* **1**, 387–396 (2013).
36. Gaztanaga, L., Marchlinski, F. E. & Betensky, B. P. Mechanisms of cardiac arrhythmias. *Rev. Esp. Cardiol.* **65**, 174–185 (2012).
37. Yu, J. K., Liang, J. A., Weinberg, S. H. & Trayanova, N. A. Computational modeling of aberrant electrical activity following revascularization with intramyocardially injected pluripotent stem cell-derived cardiomyocytes. *J. Mol. Cell Cardiol.* **162**, 97–109 (2022).
38. Jou, C. J., Spitzer, K. W. & Tristani-Firouzi, M. Blebbistatin effectively uncouples the excitation-contraction process in zebrafish embryonic heart. *Cell Physiol. Biochem.* **25**, 419–424 (2010).
39. Zhang, H., Iijima, K., Huang, J., Walcott, G. P. & Rogers, J. M. Optical mapping of membrane potential and epicardial deformation in beating hearts. *Biophys. J.* **111**, 438–451 (2016).
40. Kim, J. J. et al. Mechanism of automaticity in cardiomyocytes derived from human induced pluripotent stem cells. *J. Mol. Cell Cardiol.* **81**, 81–93 (2015).
41. Gwathmey, J. K., Hajjar, R. J. & Solaro, R. J. Contractile deactivation and uncoupling of crossbridges. Effects of 2,3-butanedione monoxime on mammalian myocardium. *Circ. Res.* **69**, 1280–1292 (1991).
42. Lerman, B. B., Markowitz, S. M., Cheung, J. W., Thomas, G. & Ip, J. E. Ventricular tachycardia due to triggered activity: role of early and delayed afterdepolarizations. *JACC Clin. Electrophysiol.* **10**, 379–401 (2024).
43. Xie, Y., Sato, D., Garfinkel, A., Qu, Z. & Weiss, J. N. So little source, so much sink: requirements for afterdepolarizations to propagate in tissue. *Biophys. J.* **99**, 1408–1415 (2010).
44. Zhang, L. et al. Derivation and high engraftment of patient-specific cardiomyocyte sheet using induced pluripotent stem cells generated from adult cardiac fibroblast. *Circ. Heart Fail.* **8**, 156–166 (2015).
45. Lian, X. et al. Directed cardiomyocyte differentiation from human pluripotent stem cells by modulating Wnt/beta-catenin signaling under fully defined conditions. *Nat. Protoc.* **8**, 162–175 (2013).
46. Kahn-Krell, A. et al. Bioreactor suspension culture: differentiation and production of cardiomyocyte spheroids from human induced pluripotent stem cells. *Front. Bioeng. Biotechnol.* **9**, 674260 (2021).
47. Tan, S. et al. Non-viral vector based gene transfection with human induced pluripotent stem cells derived cardiomyocytes. *Sci. Rep.* **9**, 14404 (2019).
48. Madden, L., Juhas, M., Kraus, W. E., Truskey, G. A. & Bursac, N. Bioengineered human myobundles mimic clinical responses of skeletal muscle to drugs. *Elife* **4**, e04885 (2015).
49. Wang, X. et al. Stem cells for myocardial repair with use of a transarterial catheter. *Circulation* **120**, S238–S246 (2009).
50. Yap, L. et al. Pluripotent stem cell-derived committed cardiac progenitors remuscularize damaged ischemic hearts and improve their function in pigs. *NPJ Regen. Med.* **8**, 26 (2023).
51. Qin, H. et al. Effects of heart isolation, voltage-sensitive dye, and electromechanical uncoupling agents on ventricular fibrillation. *Am. J. Physiol. Heart Circ. Physiol.* **284**, H1818–H1826 (2003).
52. Jayawant, A. M., Stephenson, E. R. Jr. & Damiano, R. J. Jr. 2,3-Butanedione monoxime cardioplegia: advantages over hyperkalemia in blood-perfused isolated hearts. *Ann. Thorac. Surg.* **67**, 618–623 (1999).
53. Kang, C. et al. Human organotypic cultured cardiac slices: new platform for high throughput preclinical human trials. *Sci. Rep.* **6**, 28798 (2016).
54. Ou, Q. et al. Physiological biomimetic culture system for pig and human heart slices. *Circ. Res.* **125**, 628–642 (2019).
55. Savitzky, A. & Golay, M. J. E. Smoothing and differentiation of data by simplified least squares procedures. *Anal. Chem.* **36**, 1627–1639 (1964).
56. Bayly, P. V. et al. Estimation of conduction velocity vector fields from epicardial mapping data. *IEEE Trans. Biomed. Eng.* **45**, 563–571 (1998).
57. Efimov, I. R., Huang, D. T., Rendt, J. M. & Salama, G. Optical mapping of repolarization and refractoriness from intact hearts. *Circulation* **90**, 1469–1480 (1994).
58. Tao, Z. et al. Angiotensin-1 enhanced myocyte mitosis, engraftment, and the reparability of hiPSC-CMs for treatment of myocardial infarction. *Cardiovasc. Res.* **117**, 1578–1591 (2021).

Acknowledgements

The authors thank S. Melnick and S. Salter for their expert assistance with animal management. This study was supported in part, by National Institutes of Health Grants: T32 HL007457 postdoctoral fellowship to B.G.; R01HL114120, R01HL131017, R01HL149137, U01HL134764, P01HL160476 to J.Z.; and R21HL140998, and R01EB029428 to J.M.R.

Author contributions

B.G., H.Z., J.Z., and J.M.R. developed the study protocol and designed the experiments. B.G. performed cell culture, sample preparation, instrumentation, data collection, and manuscript drafting. H.Z. performed instrumentation, data collection, and manuscript drafting. Y.W. assisted in cell culture and sample analysis. L.Y. assisted in immunostaining and manuscript revision. G.P.W. conducted animal surgery and assisted in manuscript revision. J.Z. and J.M.R. provided project leadership, funding acquisition, research environment, and manuscript revisions.

Competing interests

The authors declare no competing interests.

Additional information

Supplementary information The online version contains supplementary material available at <https://doi.org/10.1038/s41536-025-00434-x>.

Correspondence and requests for materials should be addressed to Jack M. Rogers or Jianyi Zhang.

Reprints and permissions information is available at <http://www.nature.com/reprints>

Publisher's note Springer Nature remains neutral with regard to jurisdictional claims in published maps and institutional affiliations.

Open Access This article is licensed under a Creative Commons Attribution-NonCommercial-NoDerivatives 4.0 International License, which permits any non-commercial use, sharing, distribution and reproduction in any medium or format, as long as you give appropriate credit to the original author(s) and the source, provide a link to the Creative Commons licence, and indicate if you modified the licensed material. You do not have permission under this licence to share adapted material derived from this article or parts of it. The images or other third party material in this article are included in the article's Creative Commons licence, unless indicated otherwise in a credit line to the material. If material is not included in the article's Creative Commons licence and your intended use is not permitted by statutory regulation or exceeds the permitted use, you will need to obtain permission directly from the copyright holder. To view a copy of this licence, visit <http://creativecommons.org/licenses/by-nc-nd/4.0/>.

© The Author(s) 2025